

Measurements of the induced polarization in the quasi-elastic $A(e, e'\vec{p})$ process in non-coplanar kinematics.

S.J. Paul^{a,1,*}, T. Kolar^b, T. Brecej^b, P. Achenbach^c, H. Arenhövel^c, A. Ashkenazi^a, J. Beričič^b, R. Böhm^c, D. Bosnar^d, E. Cline^e, E.O. Cohen^a, L. Debenjak^b, M.O. Distler^c, A. Esser^c, I. Friščič^{d,2}, R. Gilman^e, C. Giusti^f, M. Heilig^g, M. Hoek^c, D. Izraeli^a, S. Kegel^c, P. Klag^c, Y. Kohl^c, I. Korover^{h,a}, J. Lichtenstadt^a, I. Mardor^{a,i}, H. Merkel^c, D.G. Middleton^c, M. Mihovilović^{k,b,c}, J. Müller^c, U. Müller^c, M. Olivenboim^a, E. Piasetzky^a, J. Pochodzalla^c, G. Ron^j, B.S. Schlimme^c, M. Schoth^c, F. Schulz^c, C. Sfienti^c, S. Širca^{k,b}, R. Spreckels^c, S. Štajner^b, S. Strauch^l, M. Thiel^c, A. Tyukin^c, A. Weber^c, I. Yaron^a,

(A1 Collaboration)

^a*School of Physics and Astronomy, Tel Aviv University, Tel Aviv 69978, Israel.*

^b*Jožef Stefan Institute, 1000 Ljubljana, Slovenia.*

^c*Institut für Kernphysik, Johannes Gutenberg-Universität, 55099 Mainz, Germany.*

^d*Department of Physics, University of Zagreb, HR-10002 Zagreb, Croatia.*

^e*Rutgers, The State University of New Jersey, Piscataway, NJ 08855, USA.*

^f*Dipartimento di Fisica, Università degli Studi di Pavia and INFN, Sezione di Pavia, via A. Bassi 6, I-27100 Pavia, Italy.*

^g*Universität Konstanz, Fachbereich Physik, Universitätsstraße 10, 78464 Konstanz, Germany.*

^h*Department of Physics, NRCN, P.O. Box 9001, Beer-Sheva 84190, Israel.*

ⁱ*Soreq NRC, Yavne 81800, Israel.*

^j*Racah Institute of Physics, Hebrew University of Jerusalem, Jerusalem 91904, Israel.*

^k*Faculty of Mathematics and Physics, University of Ljubljana, 1000 Ljubljana, Slovenia.*

^l*University of South Carolina, Columbia, South Carolina 29208, USA.*

Abstract

We report measurements of the induced polarization \vec{P} of protons knocked out from ^2H and ^{12}C via the $A(e, e'\vec{p})$ reaction. We have studied the dependence of \vec{P} on two kinematic variables: the missing momentum p_{miss} and the “off-coplanarity” angle ϕ_{pq} between the scattering and reaction planes. For the full 360° range in ϕ_{pq} , both the normal (P_y) and, for the first time, the transverse (P_x) components of the induced polarization were measured with respect to the coordinate system associated with the scattering plane. P_x vanishes in coplanar kinematics, however in non-coplanar kinematics, it is on the same scale as P_y .

We find that the dependence on ϕ_{pq} is sine-like for P_x and cosine-like for P_y . For carbon, the magnitude of the induced polarization is especially large when protons are knocked out from the $p_{3/2}$ shell at very small p_{miss} . For the deuteron, the induced polarization is near zero at small $|p_{\text{miss}}|$, and its magnitude increases with $|p_{\text{miss}}|$. For both nuclei such behavior is reproduced qualitatively by theoretical results, driven largely by the spin-orbit part of the final-state interactions. However, for both nuclei, sizeable discrepancies exist between experiment and theory.

1 Introduction

Within the shell model a spin-orbit term is required in the mean-field potential of atomic nuclei in order to explain the energy splitting of the single-particle levels for reproducing the magic numbers [1–3]. The spin-orbit interaction also plays an important role in optical potentials which describe scattering processes. These have a strong influence in the final-state interactions (FSI) affecting quasi-free $A(e, e'\vec{p})$ scattering [4–8], as well as various other types of scattering processes [9–12].

In elastic ep scattering, within the one-photon-exchange approximation, the induced polarization of the proton van-

ishes. Consequently, it is the FSI which in the $A(e, e'\vec{p})$ reaction gives rise to a non-vanishing induced polarization of the knocked-out proton. In view of the fact that it is largely insensitive to details of the nucleon electromagnetic form factors, the induced polarization serves as an effective probe of FSI effects in quasi-elastic $A(e, e'\vec{p})$. Here we present measurements of the induced polarization of quasi-elastic protons from ^2H and ^{12}C over a wide range in the missing momentum, p_{miss} .

Previous measurements of the normal component, P_y , of the induced polarization have been performed at MIT-Bates on ^2H [13] at low p_{miss} and ^{12}C with large p_{miss} in coplanar kinematics [14]. Measurements of P_y were also performed on ^4He at Jefferson Lab (JLab) [15, 16] over a wide p_{miss} range.

In Ref. [14], it was found that the induced polarizations of protons knocked out from the s shell of ^{12}C show a different behavior from those knocked out of the p shell. This

*Corresponding author

Email address: paulsebouh@mail.tau.ac.il (S.J. Paul)

¹Present address: UC-Riverside, Riverside, CA 92521, USA.

²Present address: MIT-LNS, Cambridge, MA 02139, USA.

difference was attributed to the spin-orbit ($L \cdot S$) interaction. The measured values of P_y for ^2H at low p_{miss} in [13] were much smaller than those measured for other nuclei in [14–16]. All measurements prior to those reported here were restricted to almost-coplanar geometry.

The induced polarization measurements presented here were performed at the Mainz Microtron (MAMI), during four run periods from 2012–2017. Our measurements for both nuclei cover a large range in missing momentum, p_{miss} , and the full 360° range in the off-coplanarity angle, ϕ_{pq} (See Fig. 1). Calculations predict a dependence of the induced polarization on ϕ_{pq} largely due to the $L \cdot S$ interaction which hitherto has been unexplored. Our ^2H data greatly extend the range in p_{miss} compared to the previous measurements in [13], while our ^{12}C data significantly improve the statistical precision and the range in ϕ_{pq} compared to the existing data [14]. Furthermore, we measure not only the normal component, P_y , but also, for the first time, the transverse component, P_x , which vanishes in coplanar kinematics ($\phi_{pq} = 0^\circ$ or 180°). The *transferred* polarizations measured in our experiments were reported in [17–19] for ^2H and [20–22] for ^{12}C .

Section 2 describes the experimental setup, the measured reaction, and the kinematic settings. The data analysis and extraction of the induced polarization are described in Sec. 3. The details of theoretical calculations, to which we compare our data, are given in Sec. 4. We then present the data for both nuclei and their dependence on p_{miss} and ϕ_{pq} in Secs. 5 and 6, and conclude in Sec. 7.

2 Experimental setup and kinematics

The experiments were performed at MAMI using the A1 beamline and spectrometers [23]. For these measurements, a 600–690 MeV polarized continuous-wave electron beam was used. The beam current was $\approx 10 \mu\text{A}$. Due to the frequent flipping of the beam helicity (about 1 Hz), the average beam polarization in our event sample is zero, as verified by internal checks on the data.

The targets used for the ^2H and ^{12}C measurements were a 50 mm long oblong cell filled with liquid deuterium [17–19] and a set of three 0.8 mm-thick graphite foils [20–22], respectively. We also performed calibration runs using a liquid hydrogen target.

Two high-resolution, small-solid-angle spectrometers with momentum acceptances of 20–25% were used to detect the scattered electrons and knocked-out protons in coincidence. Each of these spectrometers consists of a momentum-analysing magnet system followed by a set of vertical drift chambers (VDCs) for tracking, and a scintillator system for triggering and defining the time coincidence between the two spectrometers.

The proton spectrometer was equipped with a focal-plane polarimeter (FPP) with a 3–7 cm thick carbon analyzer and a set of horizontal drift chambers (HDCs) [23, 24]. The spin-dependent scattering of the polarized proton by the carbon analyzer allows the determination of the proton polarization at the focal plane. The polarization at the interaction point

is then determined by correcting for the spin precession in the spectrometer’s magnetic field [24]. More details of the experiment can be found in [17–22].

The kinematics of the measured reactions are shown in Fig. 1. The electron’s initial and final momenta are \vec{k} and \vec{k}' respectively, which define the scattering plane of the reaction. The reaction plane is defined by the momentum transfer $\vec{q} = \vec{k} - \vec{k}'$ and the recoiling proton’s momentum \vec{p}' . We refer to the angle between the scattering plane and the reaction plane as the “off-coplanarity” angle of the reaction, denoted by ϕ_{pq} .

Following the convention of [15], we express the components of the induced polarization \vec{P} in the scattering-plane coordinate system, such that \hat{y} is normal to the scattering plane (along the direction of $\vec{k} \times \vec{k}'$), \hat{z} is along the direction of the momentum transfer \vec{q} , and $\hat{x} = \hat{y} \times \hat{z}$, forming a right-handed coordinate system.

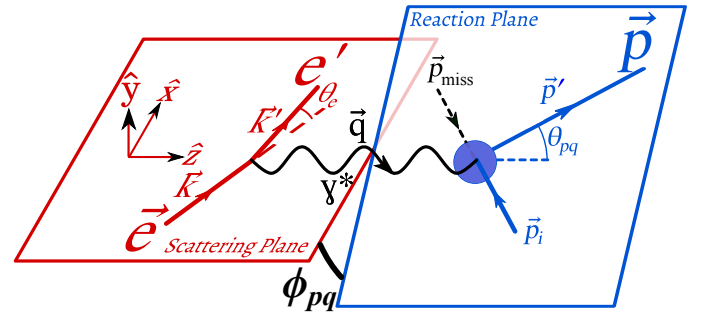


Figure 1: Kinematics of the reaction with the definitions of the kinematic variables.

The missing momentum $\vec{p}_{\text{miss}} \equiv \vec{q} - \vec{p}'$ is the recoil momentum of the residual nuclear system. Neglecting FSI, $-\vec{p}_{\text{miss}}$ is equal to the initial momentum of the emitted proton, \vec{p}_i . We conventionally define positive and negative signs for p_{miss} by the sign of $\vec{p}_{\text{miss}} \cdot \vec{q}$.

Our ^2H measurements were performed at six kinematic settings, labeled A through F, with varying ranges of p_{miss} and invariant four-momentum transfers $Q^2 = -q^2$. Settings A and F were both centered at $p_{\text{miss}} = 0$, and have $Q^2 = 0.40 \text{ (GeV/c)}^2$. Settings B and E covered large positive p_{miss} , at $Q^2 = 0.40$ and 0.65 (GeV/c)^2 , respectively. Settings C and D covered small and large negative p_{miss} , respectively, and were both at $Q^2 = 0.18 \text{ (GeV/c)}^2$. Details are given in Table 1.

Our ^{12}C measurements were taken at two kinematic settings. The first is the same Setting A of the deuteron measurements (centered near $p_{\text{miss}} = 0$, at $Q^2 = 0.40 \text{ (GeV/c)}^2$). The second is Setting G, which covered a region of large negative p_{miss} at $Q^2 = 0.18 \text{ (GeV/c)}^2$; this is similar to Setting D of the deuteron measurements, except with a different beam energy and the other kinematic variables modified accordingly³.

³In our earlier publications [20–22] on ^{12}C , this setting is referred to as Setting B. We refer to this setting as Setting G in this work in order to distinguish it from the Setting B of the deuteron measurements.

Table 1: The kinematic settings in the ${}^2\text{H}(\bar{e}, e'\bar{p})$ and ${}^{12}\text{C}(\bar{e}, e'\bar{p})$ measurements. The angles and momenta represent the central values for the two spectrometers: p_p and θ_p (p_e and θ_e) are the knocked out proton (scattered electron) momentum and scattering angles, respectively. The number of events passing the event selection cuts are also given.

		Kinematic setting						
		A	B	C	D	E	F	G
E_{beam}	[MeV]	600	600	630	630	690	690	600
Q^2	[(GeV/c) 2]	0.40	0.40	0.18	0.18	0.65	0.40	0.18
p_{miss}	[MeV/c]	-80 to 75	75 to 175	-80 to -15	-220 to -130	60 to 220	-70 to 70	-250 to -100
p_e	[MeV/c]	384	463	509	398	464	474	368
θ_e	[deg]	82.4	73.8	43.4	49.4	90.9	67.1	52.9
p_p	[MeV/c]	668	495	484	665	656	668	665
θ_p	[deg]	-34.7	-43.3	-53.3	-39.1	-33.6	-40.8	-37.8
Nucleus	shell	# of events passing cuts ($\times 10^3$)						
${}^2\text{H}$		68	19	438	201	10	232	—
${}^{12}\text{C}$	$s_{1/2}$	268	—	—	—	—	—	274
${}^{12}\text{C}$	$p_{3/2}$	160	—	—	—	—	—	436

In each of the kinematic settings presented in this work, the spectrometers' reference trajectories form a parallel reaction ($\bar{p}' \parallel \bar{q}$). However, due to the spectrometer acceptance, our data sample included reactions with θ_{pq} (the angle between \bar{p} and \bar{q}) up to $\approx 8^\circ$, with the full 360° range in the off-coplanarity angle ϕ_{pq} .

3 Data Analysis

3.1 Event selection

Software cuts were applied to the data, in order to ensure good tracking, time coincidence, and event quality. These cuts applied here are identical to those of the earlier publications [17–22] on the transferred polarization, unless otherwise noted below.

We applied additional tracking cuts to the proton's trajectory, requiring it to be within the part of the spectrometer where the precession of the proton's spin is well known and the false asymmetry could be determined using dedicated elastic ep measurements. In order to reduce false asymmetries, we also removed events where the proton would either be outside of the geometric acceptance of the detector, or produce a hit on a malfunctioning channel of the HDCs, if it had scattered in the azimuthally opposite direction. Additionally, the polar angle Θ_{FPP} of the secondary scattering was required to be greater than 8° in order to avoid spin-independent Coulomb-scattering events, and less than 23° in order to improve the stability of the false-asymmetry determination.

Following [17–19], we required the missing mass of the ${}^2\text{H}(e, e'\bar{p})$ reaction to be consistent with the mass of a neutron. For the ${}^{12}\text{C}$ sample, we distinguish between protons knocked out from the s and p shells, following [20–22], by using cuts on the missing energy, E_{miss} in the reaction, defined as [25]:

$$E_{\text{miss}} \equiv \omega - T_p - T_{11\text{B}}, \quad (1)$$

where $\omega = k^0 - k'^0$ is the energy transfer, T_p is the measured kinetic energy of the outgoing proton, and $T_{11\text{B}}$ is the calculated kinetic energy of the recoiling residual system, assuming it is ${}^{11}\text{B}$ in the ground state. For the s -shell sample, we used the cut $30 < E_{\text{miss}} < 60$ MeV, while for the p -shell sample, we used $15 < E_{\text{miss}} < 25$ MeV [20–22].

The p -shell cut accepts events in which the residual $A - 1$ system is left in one of several discrete states, including the ground-state of ${}^{11}\text{B}$ as well as a few excited states. The s -shell selection cut is much wider, comprising a broad range within the continuum of unbound residual $A - 1$ states.

3.2 Polarization fitting

Before extracting the values of P_x and P_y for ${}^2\text{H}$ and ${}^{12}\text{C}$, we first determined the false asymmetry using elastic ep events (for which the induced polarization is expected to be zero). This was accomplished by maximizing the log likelihood

$$\log \mathcal{L} = \sum_{\text{events}} \log \left[1 + \vec{A}^T \cdot \begin{pmatrix} -\sin \Phi_{\text{FPP}} \\ \cos \Phi_{\text{FPP}} \\ 0 \end{pmatrix} \right], \quad (2)$$

for the ep event sample, where Φ_{FPP} is the azimuthal angle of the secondary scattering and \vec{A} is the false asymmetry in the focal plane coordinate system, parameterized as

$$\vec{A} = \begin{pmatrix} a_0^x + a_1^x \phi_{\text{vth}} \\ a_0^y + a_1^y \theta_{\text{vth}} \\ 0 \end{pmatrix}, \quad (3)$$

where θ_{vth} and ϕ_{vth} are the incident angles of the proton trajectory extrapolated from the VDCs to the HDCs. a_0^x , a_1^x , a_0^y , and a_1^y are the fitted coefficients. We then extracted the induced polarization for ${}^2\text{H}$ and ${}^{12}\text{C}$ by maximizing the

log likelihood

$$\log \mathcal{L} = \sum_{\text{events}} \log \left[1 + (a\mathbf{S} \cdot \vec{P} + \vec{A})^T \cdot \begin{pmatrix} -\sin \Phi_{\text{FPP}} \\ \cos \Phi_{\text{FPP}} \\ 0 \end{pmatrix} \right], \quad (4)$$

where \mathbf{S} is the calculated spin-transfer matrix for the proton trajectory of the event, and a is the analyzing power of the event (as determined by [26, 27]). \vec{P} is the induced polarization. We constrain P_z to be zero in order to improve the stability of our fit. This constraint has a negligible effect on the fitted P_x and P_y except in bins with very poor statistics.

The corrections for false asymmetry are larger for P_x than for P_y ; the r.m.s. values of these corrections are ≈ 0.20 and ≈ 0.04 respectively. This is because $|A_y|$ is generally larger than $|A_x|$, and the off-diagonal terms of the spin-transfer matrix, S_{xy} and S_{yx} , dominate over the much smaller diagonal terms S_{xx} and S_{yy} . Details of the false-asymmetry determination, and the checks we used to validate its long-term stability, may be found in the supplementary material.

3.3 Systematic errors

The systematic errors in these measurements are due to a few sources, which are presented in Table 2. They are dominated by the uncertainty on the false asymmetry of the FPP. This is due to the limited statistics of the elastic ep sample used to determine this false asymmetry, and it contributes 0.012 to the systematic error on our corrected results for ${}^2\text{H}$ and ${}^{12}\text{C}$.

The analyzing power of the carbon secondary scatterer is known to about 1% in this kinematic region [24, 26, 27]. It leads to a relative error of the same size on each component of \vec{P} . The uncertainty on the precession of the proton's spin introduces an additional 0.4% relative error. The systematic error due to the uncertainty of the alignment between the HDC and the VDC detector systems was investigated to be less than 0.001, absolute, for both components. This was determined by repeating the analysis with each of the alignment parameters modified by plus or minus its uncertainty. In a similar manner, we estimate the uncertainty on both components due to the uncertainty on the kinematic settings (i.e. the beam energy and the two spectrometers' angles and momenta) to be about 0.001.

The software cuts, described in Sec. 3.1, introduce an additional absolute uncertainty of ≈ 0.006 to the overall systematic error. This was determined by performing slightly tighter cuts on each of the software cuts and then extracting the polarization as described above. The systematic uncertainty due to the cuts is then the quadrature sum of the deviations between the measured polarizations with each of the tightened cuts as compared to the standard set of cuts.

4 Calculations

For comparison, theoretical calculations of the induced polarization for ${}^2\text{H}$ and ${}^{12}\text{C}$ have been performed. For ${}^2\text{H}$ we have used a non relativistic calculation [28] including a

Table 2: Sources of systematic errors on P_x and P_y . We distinguish between sources of systematic errors that do not scale with P_y (absolute errors), and those that do (relative errors). The total systematic errors are then $\Delta P_x = \sqrt{\Delta P_{x,\text{abs}}^2 + (\Delta P_{x,\text{rel}} P_x)^2}$ and similarly for ΔP_y .

	$\Delta P_{x,\text{abs}}$	$\Delta P_{y,\text{abs}}$	$\Delta P_{xy,\text{rel}}$
False asymmetry	0.010	0.012	—
Software cuts	0.005	0.006	—
Detector alignment	< 0.001	< 0.001	—
Kinematic setting	0.001	0.001	—
Precession	—	—	0.4%
Analyzing power	—	—	1.0%
Total	0.011	0.013	1.1%

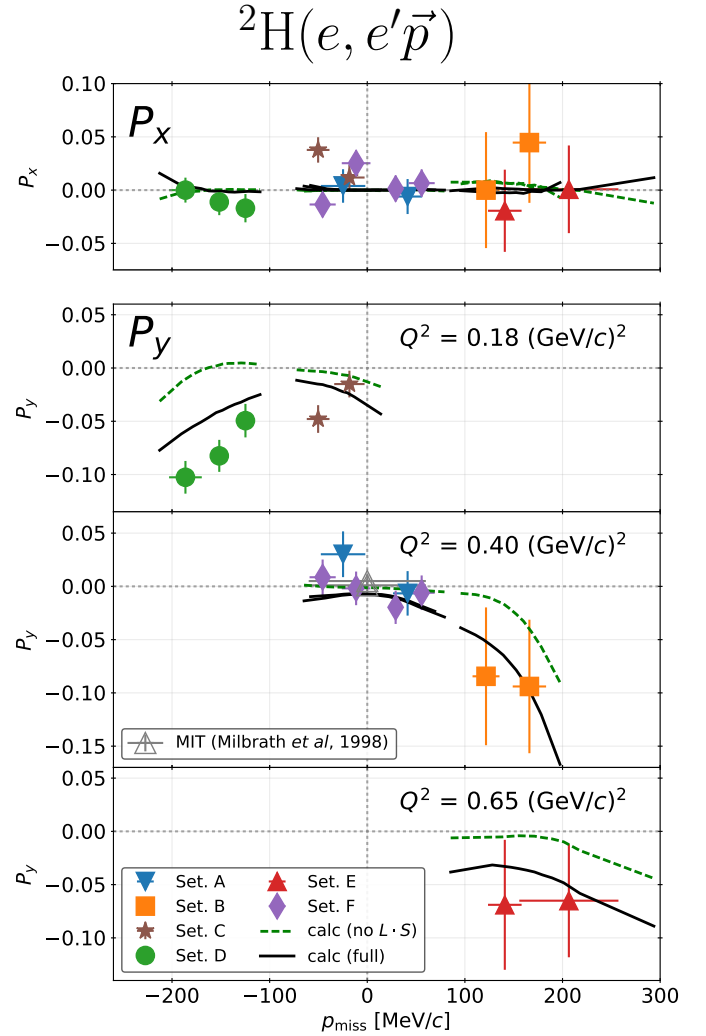


Figure 2: The measured components of the induced polarization for ${}^2\text{H}$, P_x (top panel) and P_y (three lower panels for each Q^2), as functions of the missing momentum. Different symbols (color online) represent different kinematic settings as shown in the inset of the lowest panel. Grey open triangles indicate the measurements from MIT-Bates [13], taken at $Q^2 = 0.38$ and 0.50 (GeV/c^2), both with p_{miss} centered at zero. The uncertainties shown are statistical only. Systematic errors are discussed in Sec. 3.3. Theoretical results with (without) the $L \cdot S$ part of the interaction are shown as solid black (dashed, green online) curves.

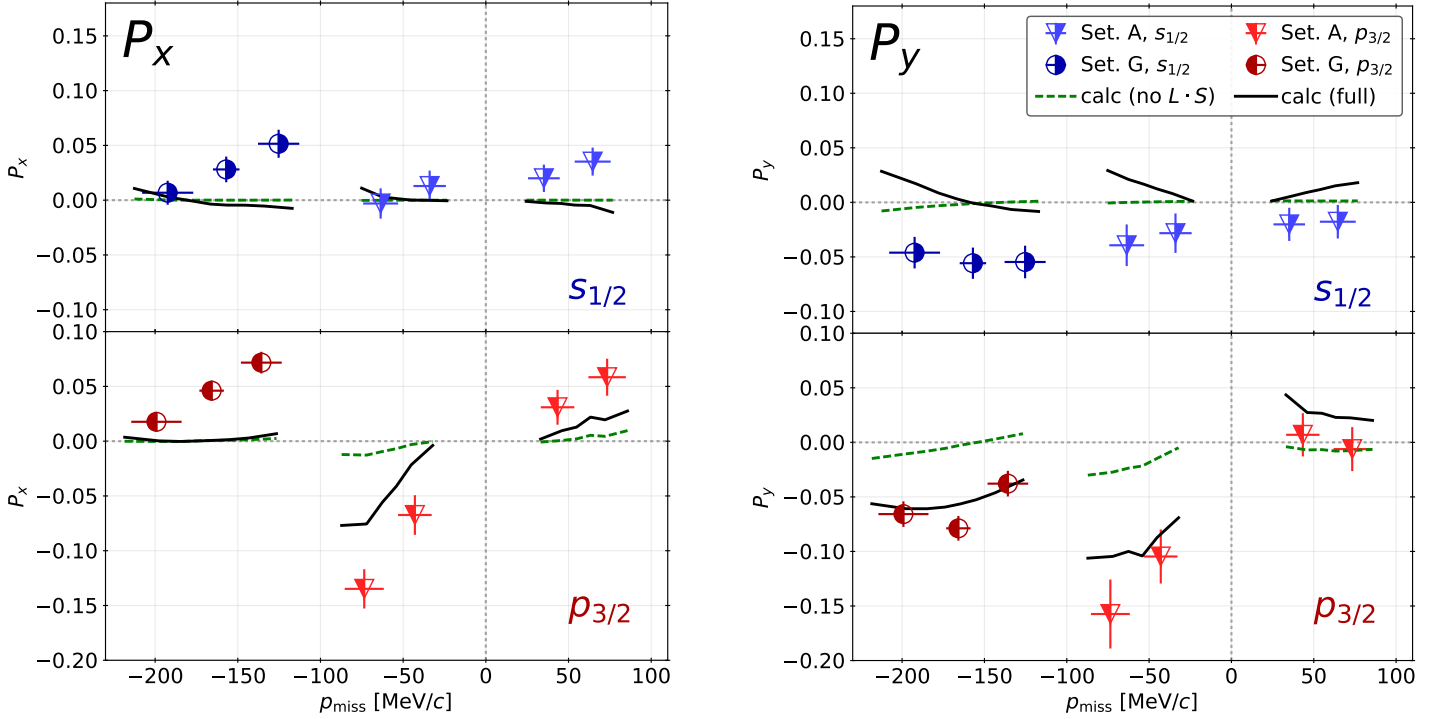
$^{12}\text{C}(e, e'\vec{p})$


Figure 3: The measured induced-polarization components, P_x (left panel) and P_y (right panel) for ^{12}C as functions of the missing momentum compared to theory. Triangles (circles) refer to kinematic Setting A (G). Symbols that are open on the left (right) side refer to s -shell (p -shell) removals, and are colored blue (red) online. The calculations with (without) the $L \cdot S$ potential are shown in solid black (dashed, green online) curves.

realistic NN -potential, meson-exchange (MEC) and isobar (IC) currents, and relativistic contributions (RC) of leading order. For the bound and scattering states the realistic Argonne V_{18} potential [29] has been taken. As nucleon electromagnetic form factors we used the parameterizations from [30].

For ^{12}C , calculations were performed using a program [7] based on the relativistic distorted-wave approximation (RDWIA) where the FSI between the outgoing proton and the residual nucleus are described by a phenomenological relativistic optical potential. The original program [7] was modified [22] in order to account for non-coplanar kinematics, by including all relevant structure functions [6]. In the RDWIA calculations, only the one-body electromagnetic nuclear current is included. We chose the current operator corresponding to the $cc2$ definition [31], and we used the same parameterization of the nucleon form factors [30] as in the ^2H calculations. The relativistic proton bound-state wave functions were obtained from the NL-SH parametrization [32] and the scattering states from the so-called “democratic” parameterization of the optical potential [33].

We found that for both nuclei, the calculated induced polarization has very little sensitivity to the details of the nucleon form factors. A change of 10% to the form-factor ratio G_E/G_M in the calculations affects the induced polarization by less than 0.005.

In order to examine the influence of the $L \cdot S$ interaction

on the induced polarization, we repeated these calculations while switching off this part of the potential. As we will show in Secs. 5 and 6, the $L \cdot S$ interaction is the dominant source of the induced polarization.

5 Missing-momentum dependence

We partitioned the ^2H data for each kinematic setting into bins by p_{miss} and extracted P_x and P_y for each bin separately, and present the results in Fig. 2. The results for P_x (top panel) are consistent with zero within error. The extracted values of P_y , on the other hand, are near zero at small p_{miss} and deviate from zero at large $|p_{\text{miss}}|$. This is consistent with earlier measurements of P_y from MIT [13] (grey pentagons in Fig. 2), which show that for $|p_{\text{miss}}| < 60$ MeV/ c , the values of P_y are consistent with zero. The reason for this feature lies in the fact that for $p_{\text{miss}} = 0$, which is the ideal quasi-free case, the influence of FSI is very small, almost zero.

In order to compare with theory, we calculated P_x and P_y for a sample of the ^2H events which reflect the distribution of events in the phase space at each kinematic setting and took the average value by bins in p_{miss} , as shown in Fig. 2 by solid black curves. The calculations for P_x vanish, while those for P_y are near zero at $p_{\text{miss}} \approx 0$, but they become increasingly negative at increasing $|p_{\text{miss}}|$. The P_y calcu-

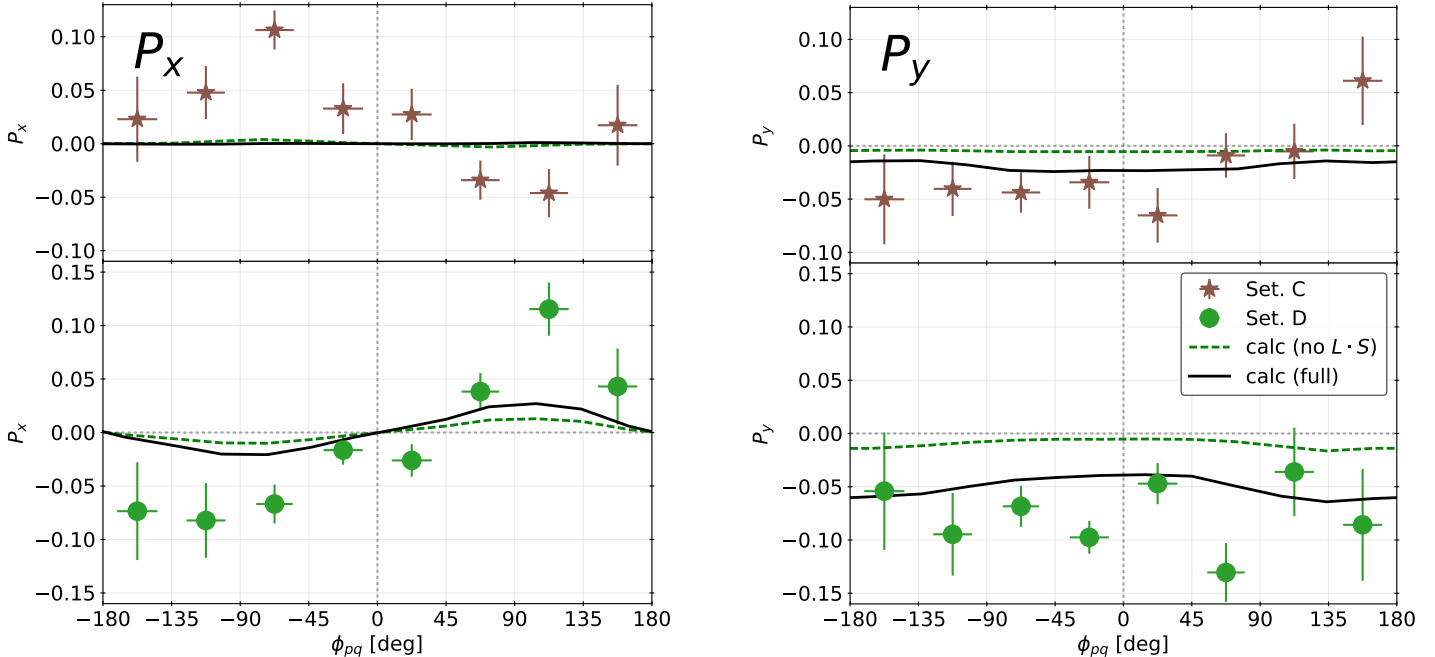
${}^2\text{H}(e, e'\vec{p})$


Figure 4: Comparison of the ϕ_{pq} dependence of the measured induced polarization components P_x (left panels) and P_y (right panels) for ${}^2\text{H}$ to the theory for selected kinematic settings. Symbols are explained in the inset of the right bottom panel. The calculations with (without) the $L \cdot S$ potential are shown as the solid black (dashed, green online) curves.

lations match the data very well except at large negative p_{miss} (Setting D).

The theoretical results obtained by switching off the $L \cdot S$ interaction are presented as dashed (green online) curves in Fig. 2. Similar to the complete calculation, the calculated P_x without the $L \cdot S$ interaction is essentially zero. For P_y , the corresponding difference between the full and no- $L \cdot S$ calculation is large, indicating the important influence of the $L \cdot S$ interaction on P_y . The theory appears to describe the data quite well except for P_y in Settings C and D.

For ${}^{12}\text{C}$ we performed the same polarization-fitting procedure and present the results in Fig. 3. Unlike in our results for ${}^2\text{H}$, the measured P_x for ${}^{12}\text{C}$ is non-zero when binned in p_{miss} . While a non-zero P_x at coplanar kinematics is theoretically forbidden (see [5]), our data are not restricted to coplanarity, and therefore we do not require P_x to be zero. The non-zero values of P_x in the left panels of Fig. 3 reflect the distributions of other kinematic variables (such as ϕ_{pq}) within each p_{miss} bin. We will discuss this in further detail in Sec. 6, where we will show that P_x is highly dependent on ϕ_{pq} .

The component P_y for the s -shell data (upper part of the right panel of Fig. 3) appears to be nearly constant at $P_y \approx -0.04$ as function of p_{miss} , while the p -shell data show a significant variation with p_{miss} .

A comparison of our ${}^{12}\text{C}$ data for P_y with the earlier MIT measurements [14] is shown in the supplementary material. We found that our data are consistent with the latter when restricting the range of ϕ_{pq} in our data sample to match

that of [14] (i.e., near 180°) and comparing them at the same $|p_{\text{miss}}|$.

The calculations for the ${}^{12}\text{C}$ events using samples of s -shell and p -shell data from both kinematic sets, with (without) the $L \cdot S$ part of the optical potential, as functions of the binned p_{miss} , are shown in Fig. 3 as solid black (dashed, green online) curves. The results including the $L \cdot S$ term show much larger deviations from zero than the results without it, indicating that most of the deviation from zero originates from the $L \cdot S$ term.

The P_x curves are non-zero, and reflect the asymmetries of the kinematics of the accepted events. For P_y , the full-potential calculation (solid black) curves are above the measured data points by up to 0.05, and in some cases, the calculations have the opposite sign of the measured P_y .

6 Dependence on off-coplanarity

In order to examine the ϕ_{pq} dependence of P_x and P_y , we performed the fits to the data in bins of ϕ_{pq} .

The results for ${}^2\text{H}$ at the negative- p_{miss} kinematic settings (C and D) are shown in Fig. 4. These are the only two settings for which we observe a significant ϕ_{pq} dependence in the data (for completeness, the results for the other settings are shown in the supplementary material). In both of these two settings, the P_x have a sine-shaped dependence on ϕ_{pq} , albeit with opposite signs for the two settings. In all six of the ${}^2\text{H}$ settings, P_y shows no statistically significant variation with respect to ϕ_{pq} .

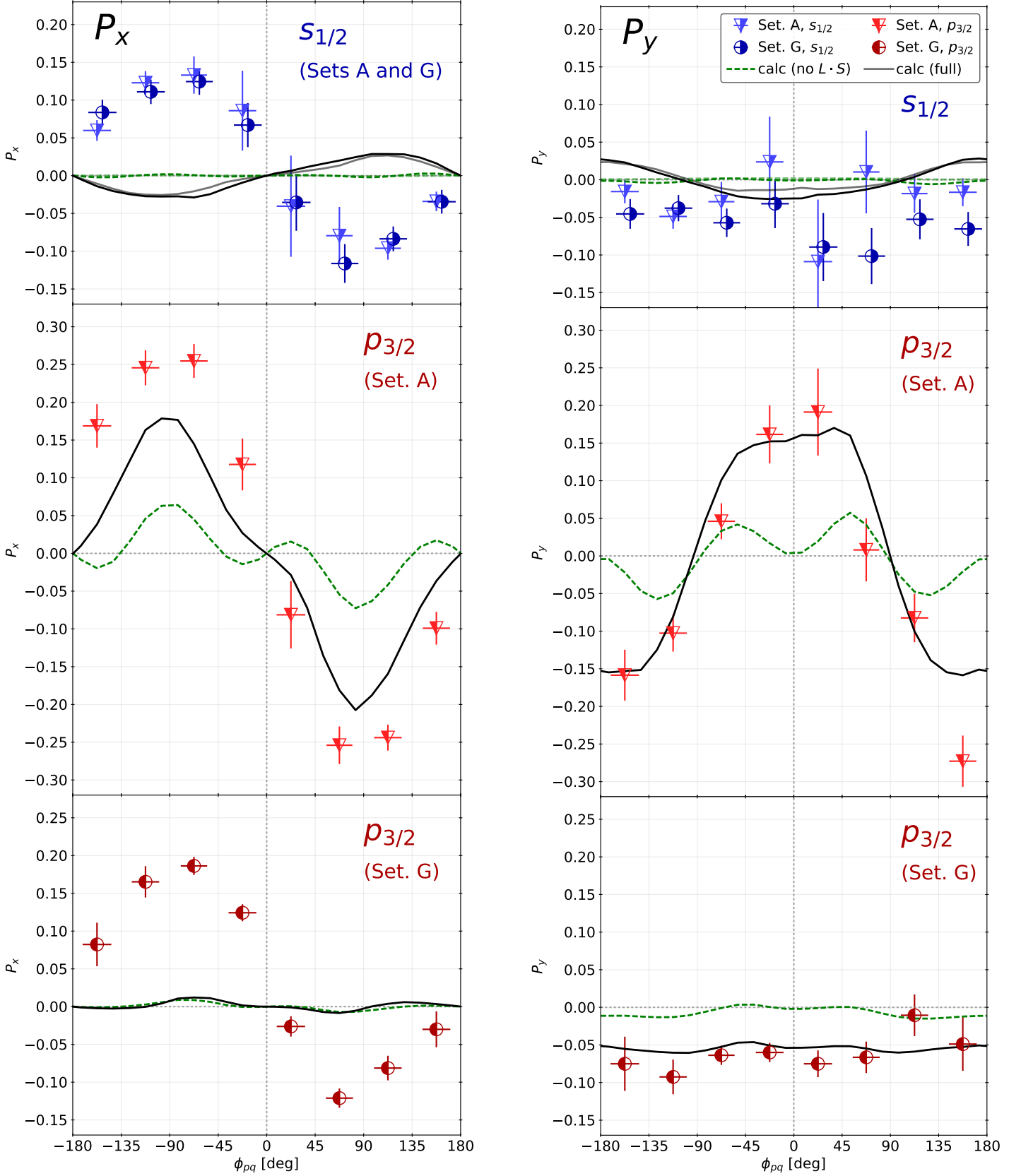
$^{12}\text{C}(e, e'\vec{p})$


Figure 5: For ^{12}C , the ϕ_{pq} dependence of the measured polarization components P_x (left panels) and P_y (right panels) compared to theory. These are shown for s -shell knockout for both kinematic settings (top panels), and for p -shell knockout at small p_{miss} (Setting A, middle panels) and large negative p_{miss} (Setting G, bottom panels). Calculations with (without) the $L \cdot S$ part of the optical potential are shown as solid black (dashed, green online) curves. In the top panels, the curves for Setting A are shown in grey (light green online for no- $L \cdot S$) in order to contrast with those of Setting G.

The theory predicts for P_x for Setting C an almost vanishing ϕ_{pq} dependence in contrast to the data, while for Setting D a small sine-shaped behavior is obtained, however, with a much smaller amplitude than the much more pronounced data. For P_y the agreement with the data appears to be better. For both settings, there is only a small variation in P_y with respect to ϕ_{pq} , and its amplitude is larger for Setting D than for Setting C. Furthermore, one notes for both components a sizeable contribution for the case where the $L \cdot S$ -part is switched-off.

The results for ^{12}C are shown in Fig. 5. The P_x results have a negative sine-like shape, with nearly the same amplitude for s -shell knockout from both kinematic settings as well as for p -shell knockout at large negative p_{miss} (Setting G); the latter however has a more pronounced asymmetry between the regions of positive and negative ϕ_{pq} . A possible explanation for this asymmetry is that the accepted events with positive and negative ϕ_{pq} have slightly different kinematics from one another, due to acceptance effects. For p -shell knockout at small p_{miss} (Setting A) the amplitude is considerably larger. In near-coplanar kinematics ($\phi_{pq} \approx 0^\circ$ or $\pm 180^\circ$), the measured P_x is consistent with zero.

The component P_y exhibits a similar ϕ_{pq} dependence in s -shell knockout (top right panel) and p -shell knockout at large $|p_{\text{miss}}|$ (Setting G, lowest right panel) being approximately constant at -0.05 . However, for p -shell knockout at small p_{miss} (Setting A, middle right panel), P_y has a large cosine-like ϕ_{pq} dependence.

The theoretical results with (without) the $L \cdot S$ part of the optical potential are displayed in Fig. 5 as solid black (dashed, green online) curves. The calculations predict in contrast to the data a much smaller P_x for the s shell than shown by the data, moreover with the opposite sign. For the p -shell knockout at Setting G (left lowest panel) P_x is almost vanishing. For the p -shell knockout at Setting A (left middle panel), P_x shows a distorted sine-like dependence, similar to the data, but with an about 35% smaller amplitude.

For P_y (right panels) the theory agrees much better with the data than for P_x . For s -shell knockout there appears to be an offset by about 0.05 compared to the data. In particular for ϕ_{pq} near $\pm 180^\circ$, the theory predicts a positive value in contrast to the data. On the other hand, for p -shell knockout (middle and lower right panels) the agreement is quite good. For the p -shell knockout in Setting A, the amplitude of P_y increases as p_{miss} approaches zero, both in the data and in the calculations, as shown in the supplementary material.

When performing the calculations with the $L \cdot S$ term of the potential switched off (dashed curves, green online), both components of the induced polarization are nearly zero, except for p -shell knockout at p_{miss} near zero (Setting A). In that region, the no- $L \cdot S$ curves are not close to zero and show a stronger oscillatory behavior but with a smaller amplitude, about one third of the one with the $L \cdot S$ term included.

7 Conclusions

We have measured in $A(e, e'\vec{p})$ the induced polarization components P_x and P_y for both ^{12}C and ^2H , greatly extending the kinematic range of previous P_y -only measurements for both nuclei. Within the regions where our kinematics overlap in p_{miss} and ϕ_{pq} with the existing experiments, our data are consistent with the other experiments. We find that in the regions where the induced polarization depends on ϕ_{pq} , the dependence is sine-like for P_x and cosine-like for P_y .

For both nuclei, P_x is consistent with zero for near-coplanar events, as expected. However, the theoretical results for P_x for both nuclei predict a considerably smaller P_x than reflected in the data, moreover in some cases with the opposite sign.

For ^2H , the induced polarization is near zero at small $|p_{\text{miss}}|$. P_x shows no significant deviation from zero except at the negative- p_{miss} settings, where it shows a dependency on ϕ_{pq} . P_y becomes increasingly negative at larger $|p_{\text{miss}}|$. This is consistent with the calculations, although the data show a significantly steeper decrease at negative p_{miss} . P_y shows no significant dependence on ϕ_{pq} at any of the kinematic settings in this work. In the calculations, most of the deviation of P_y from zero comes from the $L \cdot S$ interaction.

For ^{12}C , the measured ϕ_{pq} dependence of P_x shows a pronounced negative sine-like shape in both s - and p -shell knockout which is not reflected in the theoretical results. For the s -shell knockout, P_y has no strong dependence on either p_{miss} nor ϕ_{pq} . However, for p -shell knockout from ^{12}C , P_y is strongly dependent on ϕ_{pq} at small p_{miss} , and P_x is also more strongly dependent on ϕ_{pq} than in any other region explored in this work. This behavior at small p_{miss} for p -shell knockout is reproduced by the calculations, wherein the large dependence on ϕ_{pq} is mainly due to the spin-orbit term of the FSI.

The new data presented in this work provide a rich opportunity to further fine-tune the $L \cdot S$ part of the optical and NN potentials.

8 Acknowledgements

We would like to thank the Mainz Microtron operators and technical crew for the excellent operation of the accelerator. This work is supported by the Israel Science Foundation (Grants 390/15, 951/19) of the Israel Academy of Arts and Sciences, by the Israel Ministry of Science, Technology and Spaces, by the PAZY Foundation (Grant 294/18), by the Deutsche Forschungsgemeinschaft (Collaborative Research Center 1044), by the U.S. National Science Foundation (PHY-1205782, PHY-1505615), and by the Croatian Science Foundation Project No. 8570. We acknowledge the financial support from the Slovenian Research Agency (research core funding No. P1-0102).

9 Supplementary Material

Supplementary material may be found at [insert.url.here.com](#).

10 References

References

- [1] M. G. Mayer, Nuclear configurations in the spin-orbit coupling model. i. empirical evidence, *Phys. Rev.* 78 (1950) 16–21. doi:[10.1103/PhysRev.78.16](https://doi.org/10.1103/PhysRev.78.16).
- [2] O. Sorlin, M.-G. Porquet, Nuclear magic numbers: New features far from stability, *Progress in Particle and Nuclear Physics* 61 (2) (2008) 602 – 673. doi:<https://doi.org/10.1016/j.pnpnp.2008.05.001>.
- [3] O. Haxel, J. H. D. Jensen, H. E. Suess, On the "magic numbers" in nuclear structure, *Phys. Rev.* 75 (1949) 1766–1766. doi:[10.1103/PhysRev.75.1766.2](https://doi.org/10.1103/PhysRev.75.1766.2).
- [4] S. Boffi, C. Giusti, F. Pacati, Spin-orbit distortion of the emerging nucleon in quasi-free electron scattering, *Nuclear Physics A* 336 (3) (1980) 437 – 445. doi:[https://doi.org/10.1016/0375-9474\(80\)90220-1](https://doi.org/10.1016/0375-9474(80)90220-1).
- [5] C. Giusti, F. D. Pacati, Complete Determination of Scattering Amplitudes and Nucleon Polarization in Electromagnetic Knockout Reactions, *Nucl. Phys. A* 504 (1989) 685–711. doi:[10.1016/0375-9474\(89\)90003-1](https://doi.org/10.1016/0375-9474(89)90003-1).
- [6] S. Boffi, C. Giusti, F. d. Pacati, M. Radici, *Electromagnetic Response of Atomic Nuclei*, Vol. 20 of Oxford Studies in Nuclear Physics, Clarendon Press, Oxford UK, 1996.
- [7] A. Meucci, C. Giusti, F. D. Pacati, Relativistic corrections in (e, e-prime p) knockout reactions, *Phys. Rev. C* 64 (2001) 014604. arXiv:[nucl-th/0101034](https://arxiv.org/abs/nuc1-th/0101034), doi:[10.1103/PhysRevC.64.014604](https://doi.org/10.1103/PhysRevC.64.014604).
- [8] J. R. Vignote, M. C. Martínez, J. A. Caballero, E. Moya de Guerra, J. M. Udias, $a(\bar{e}, e'p)b$ responses: From bare nucleons to complex nuclei, *Phys. Rev. C* 70 (2004) 044608. doi:[10.1103/PhysRevC.70.044608](https://doi.org/10.1103/PhysRevC.70.044608).
- [9] L. L. Lee, J. P. Schiffer, Experimental evidence for j dependence of the angular distribution from (d, p) reactions, *Phys. Rev. Lett.* 12 (1964) 108–110. doi:[10.1103/PhysRevLett.12.108](https://doi.org/10.1103/PhysRevLett.12.108).
- [10] J. P. Schiffer, L. L. Lee, A. Marinov, C. Mayer-Böricke, Dependence of the angular distribution of the (d, p) reaction on the total angular-momentum transfer. ii, *Phys. Rev.* 147 (1966) 829–835. doi:[10.1103/PhysRev.147.829](https://doi.org/10.1103/PhysRev.147.829).
- [11] Y. Horikawa, M. Thies, F. Lenz, The δ -nucleus spin-orbit interaction in π -nucleus scattering, *Nuclear Physics A* 345 (2) (1980) 386 – 408. doi:[https://doi.org/10.1016/0375-9474\(80\)90346-2](https://doi.org/10.1016/0375-9474(80)90346-2).
- [12] S. Watanabe, High energy scattering of deuterons by complex nuclei, *Nuclear Physics* 8 (1958) 484 – 492. doi:[https://doi.org/10.1016/0029-5582\(58\)90180-9](https://doi.org/10.1016/0029-5582(58)90180-9).
- [13] B. D. Milbrath, J. I. McIntyre, C. S. Armstrong, D. H. Barkhuff, W. Bertozzi, J. Chen, others (Bates FPP Collaboration), A Comparison of polarization observables in electron scattering from the proton and deuteron, *Phys. Rev. Lett.* 80 (1998) 452–455, [Erratum: *Phys. Rev. Lett.* 82, 2221 (1999)]. arXiv:[nucl-ex/9712006](https://arxiv.org/abs/nuc1-ex/9712006), doi:[10.1103/PhysRevLett.80.452](https://doi.org/10.1103/PhysRevLett.80.452), [10.1103/PhysRevLett.82.2221](https://doi.org/10.1103/PhysRevLett.82.2221).
- [14] R. Woo, et al., Measurement of the Induced Proton Polarization P_n in the $^{12}\text{C}(e, e'p)$ Reaction, *Physical Review Letters* 80. doi:[10.1103/PhysRevLett.80.456](https://doi.org/10.1103/PhysRevLett.80.456).
- [15] S. Strauch, S. Dieterich, et al., Polarization transfer in the $^4\text{He}(\bar{e}, e'p)^3\text{H}$ reaction up to $Q^2 = 2.6$ (GeV/c) 2 , *Phys. Rev. Lett.* 91 (2003) 052301. doi:[10.1103/PhysRevLett.91.052301](https://doi.org/10.1103/PhysRevLett.91.052301).
- [16] S. P. Malace, M. Paolone, S. Strauch, I. Albayrak, J. Arrington, B. L. Berman, E. J. Brash, B. Briscoe, A. Camsonne, J.-P. Chen, et al., Precise Extraction of the Induced Polarization in the $^4\text{He}(\bar{e}, e'p)^3\text{H}$ Reaction, *Physical Review Letters* 106 (5). doi:[10.1103/physrevlett.106.052501](https://doi.org/10.1103/physrevlett.106.052501).
- [17] I. Yaron, D. Izraeli, et al., Polarization-transfer measurement to a large-virtuality bound proton in the deuteron, *Phys. Lett. B* 769 (2017) 21–24. doi:[10.1016/j.physletb.2017.01.034](https://doi.org/10.1016/j.physletb.2017.01.034).
- [18] D. Izraeli, I. Yaron, et al., Components of polarization-transfer to a bound proton in a deuteron measured by quasi-elastic electron scattering, *Phys. Lett. B* 781 (2018) 107–111. arXiv:[1801.01306](https://arxiv.org/abs/1801.01306), doi:[10.1016/j.physletb.2018.03.063](https://doi.org/10.1016/j.physletb.2018.03.063).
- [19] S. Paul, D. Izraeli, T. Breceelj, I. Yaron, et al., Polarization-transfer measurements in deuteron quasi-elastic anti-parallel kinematics, *Phys. Lett. B* 795C (2019) 599–605. arXiv:[1905.05594](https://arxiv.org/abs/1905.05594), doi:[10.1016/j.physletb.2019.07.002](https://doi.org/10.1016/j.physletb.2019.07.002).
- [20] D. Izraeli, T. Breceelj, et al., Measurement of polarization-transfer to bound protons in carbon and its virtuality dependence, *Phys. Lett. B* 781 (2018) 95–98. arXiv:[1711.09680](https://arxiv.org/abs/1711.09680), doi:[10.1016/j.physletb.2018.03.027](https://doi.org/10.1016/j.physletb.2018.03.027).
- [21] T. Breceelj, S. J. Paul, T. Kolar, et al., Polarization transfer to bound protons measured by quasielastic electron scattering on ^{12}C , *Phys. Rev. C* 101 (2020) 064615. doi:[10.1103/PhysRevC.101.064615](https://doi.org/10.1103/PhysRevC.101.064615).
- [22] T. Kolar, S. Paul, T. Breceelj, et al., Comparison of recoil polarization in the $^{12}\text{C}(\bar{e}, e'p)$ process for protons extracted from s and p shell, To be published arXiv:[2007.14985](https://arxiv.org/abs/2007.14985).
- [23] K. Blomqvist, et al., The three-spectrometer facility at MAMI, *Nucl. Instrum. and Meth. A* 403 (2–3) (1998) 263 – 301. doi:[10.1016/S0168-9002\(97\)01133-9](https://doi.org/10.1016/S0168-9002(97)01133-9).
- [24] T. Pospischil, et al., The focal plane proton-polarimeter for the 3-spectrometer setup at MAMI, *Nucl. Instrum. Methods. Phys. Res., Sect. A* 483 (3) (2002) 713 – 725. doi:[10.1016/S0168-9002\(01\)01955-6](https://doi.org/10.1016/S0168-9002(01)01955-6).
- [25] D. Dutta, et al., Quasielastic ($e, e'p$) reaction on ^{12}C , ^{56}Fe , and ^{197}Au , *Phys. Rev. C* 68 (2003) 064603. doi:[10.1103/PhysRevC.68.064603](https://doi.org/10.1103/PhysRevC.68.064603).
- [26] E. Aprile-Giboni, R. Hausammann, E. Heer, R. Hess, C. Lechanoine-Leluc, W. Leo, S. Morenzoni, Y. Onel, D. Rapin, Proton-carbon effective analyzing power between 95 and 570 MeV, *Nucl. Instrum. Meth.* 215 (1983) 147–157. doi:[10.1016/0167-5087\(83\)91302-9](https://doi.org/10.1016/0167-5087(83)91302-9).
- [27] M. W. McNaughton, et al., The p-C analyzing power between 100 and 750 MeV, *Nucl. Instrum. Meth. A* 241 (1985) 435–440. doi:[10.1016/0168-9002\(85\)90595-9](https://doi.org/10.1016/0168-9002(85)90595-9).

- [28] H. Arenhövel, W. Leidemann, E. L. Tomusiak, General survey of polarization observables in deuteron electrodisintegration, *Eur. Phys. J. A* 23 (2005) 147–190. doi:[10.1140/epja/i2004-10061-5](https://doi.org/10.1140/epja/i2004-10061-5).
- [29] R. B. Wiringa, V. G. J. Stoks, R. Schiavilla, Accurate nucleon-nucleon potential with charge-independence breaking, *Phys. Rev. C* 51 (1995) 38–51. doi:[10.1103/PhysRevC.51.38](https://doi.org/10.1103/PhysRevC.51.38).
- [30] J. C. Bernauer, M. O. Distler, J. Friedrich, T. Walcher, P. Achenbach, C. Ayerbe-Gayoso, et al., Electric and magnetic form factors of the proton, *Phys. Rev. C* 90 (1) (2014) 015206. doi:[10.1103/PhysRevC.90.015206](https://doi.org/10.1103/PhysRevC.90.015206).
- [31] T. De Forest, Off-shell electron-nucleon cross sections: The impulse approximation, *Nuclear Physics A* 392 (2) (1983) 232 – 248. doi:[https://doi.org/10.1016/0375-9474\(83\)90124-0](https://doi.org/10.1016/0375-9474(83)90124-0).
- [32] M. Sharma, M. Nagarajan, P. Ring, Rho meson coupling in the relativistic mean field theory and description of exotic nuclei, *Phys. Lett. B* 312 (4) (1993) 377 – 381. doi:[https://doi.org/10.1016/0370-2693\(93\)90970-S](https://doi.org/10.1016/0370-2693(93)90970-S).
- [33] E. D. Cooper, S. Hama, B. C. Clark, Global dirac optical potential from helium to lead, *Phys. Rev. C* 80 (2009) 034605. doi:[10.1103/PhysRevC.80.034605](https://doi.org/10.1103/PhysRevC.80.034605).

Supplementary Materials

S.1 Determination of false asymmetries using elastic ep measurements

In order to determine the false asymmetry of the polarimeter, we performed measurements using a hydrogen target, for which the induced polarization is expected to vanish. The settings for both spectrometers were similar to Setting A, except that we scanned through several proton-momentum settings in order to cover a large range of the focal plane with ep data (for which the proton's momentum and angle are correlated with one another). The event samples from each of the proton spectrometer momentum settings were combined.

As noted in the paper, we performed the fit for the false asymmetry by maximizing the log likelihood

$$\log \mathcal{L} = \sum_{\text{events}} \log \left[1 + \vec{A}^T \cdot \begin{pmatrix} -\sin \Phi_{\text{FPP}} \\ \cos \Phi_{\text{FPP}} \\ 0 \end{pmatrix} \right], \quad (5)$$

for the ep event sample, where Φ_{FPP} is the azimuthal angle of the secondary scattering and \vec{A} is the false asymmetry in the focal plane coordinate system, parameterized as

$$\vec{A} = \begin{pmatrix} a_0^x + a_1^x \phi_{\text{vth}} \\ a_0^y + a_1^y \theta_{\text{vth}} \\ 0 \end{pmatrix}, \quad (6)$$

where θ_{vth} and ϕ_{vth} are the incident angles of the proton trajectory extrapolated from the VDCs to the HDCs. a_0^x , a_1^x , a_0^y , and a_1^y are the fitted coefficients.

To validate the fits for the false asymmetry, we divided the ep event sample into slices by three of the proton kinematic variables: its momentum (divided by the reference momentum of the spectrometer setting), its polar angle θ_p , and its azimuthal angle ϕ_p , and performed fits for the components P_x^{FPP} and P_y^{FPP} of the induced polarization in the focal-plane coordinates for each slice. These fits were performed with (blue filled circles, connected by solid lines) and without (orange open circles, connected by dashed lines) the corrections for the false asymmetry, as shown in Fig. S.1. The corrected values of P_x^{FPP} (top) and P_y^{FPP} (bottom) are consistent with zero. The uncorrected values of P_x^{FPP} are slightly higher than zero, whereas those of P_y^{FPP} are large, especially when $|\phi_p - 180^\circ|$ is large, indicating that the corrections for the former are small while those of the latter are large.

The ep sample used for the false-asymmetry determination were taken in 2012, just before the ^2H measurements at Settings A-D were obtained. We used three checks to validate the long-term stability of the false-asymmetry parameterization between the four run periods. First, we compared the ^{12}C data for at Setting G taken in the 2015 run period with the data taken at the same setting during the 2017 run period, and found that these are consistent within error of each other. Second, the ^2H data at Settings A and F (which are very similar kinematics to one another), taken in 2012 and 2016 respectively, are consistent with one another within error. Finally, we checked that the results for P_x (in interaction-point coordinates) at ϕ_{pq} near 0° and $\pm 180^\circ$ in all four run periods are consistent with zero within error, as expected. Together, these checks indicate that the false asymmetry is stable between the run periods.

S.2 Comparison of ^{12}C data to MIT results

In Fig. S.2, we compare our ^{12}C measurements (half-filled triangles and circles) to those from MIT [14] (filled diamonds) which were taken at ϕ_{pq} centered at 180° . For this comparison, we selected only the events with $|\phi_{pq}| > 135^\circ$ for consistency with the kinematics of the MIT measurements. Following [14], we plot our s -shell data separately for two bins in E_{miss} : 29 to 39 MeV/ c and 39 to 50 MeV/ c . The data are shown in bins of $|p_{\text{miss}}|$.

For the p -shell knockout, both our high- $|\phi_{pq}|$ data and those of [14] have large negative P_y at small $|p_{\text{miss}}|$ and small negative P_y at large $|p_{\text{miss}}|$. We fitted our data and those of [14] to a straight line and show this fit as a dashed green line in the top panel of Fig. S.2. Both datasets are consistent with the fit within error ($\chi^2 = 3.3$ with 9 degrees of freedom; $p_{\text{val}} = 0.95$).

For the s -shell knockout, we took the weighted average (horizontal-line fit) of P_y for our measurements and those of [14] and obtained $P_y^{\text{avg}} = -0.03$. This is shown as a purple dashed line in the middle and bottom panels of Fig. S.2. Both our data and those of [14] are consistent within uncertainty of this value ($\chi^2 = 19.7$, with 21 d.o.f.; $p_{\text{val}} = 0.54$).

S.3 ϕ_{pq} -dependence of the induced polarization in ^2H

In Fig. S.3, we show the dependence of P_x and P_y on ϕ_{pq} for all six kinematic settings in both the data and the calculations. For P_x , there is no statistically significant variation in the data except in Settings C and D, as noted in the paper. P_y shows no significant dependence on ϕ_{pq} , while the calculation-curves are nearly flat for all six settings except Setting D (large negative p_{miss} , at $Q^2 = 0.18$ (GeV/ c) 2).

S.4 ϕ_{pq} -dependence of the induced polarization in ^{12}C at small p_{miss}

As noted in the paper, the data at Setting A for p -shell knockout has a large ϕ_{pq} -dependence for P_y , while the rest of the data show no such dependence. This was observed in both the data and the calculations. We also found that P_x for this subset of the data is also larger in magnitude than for the rest of the data.

In order to determine if this ϕ_{pq} dependence is correlated with p_{miss} , we partitioned the p -shell data into slices by p_{miss} , and plot the ϕ_{pq} dependence for each slice in Figs. S.4 (Setting G) and S.5 (Setting A). A purple dotted curve represents a fit to the data in each slice by the equations

$$P_x = a_x + b_x \sin \phi_{pq} \quad (7)$$

and

$$P_y = a_y + b_y \cos \phi_{pq}. \quad (8)$$

The values of b_x and b_y (which consider the ϕ_{pq} dependence of P_x and P_y) are shown in Fig. S.6. The fit parameter b_x is small at large negative p_{miss} (Setting G), and increases in absolute value to a negative plateau as p_{miss} approaches 0 in Setting A. The fit parameter b_y is near zero for large p_{miss} (Setting G) and reaches a sharp peak at $p_{\text{miss}} = 0$ (middle of Setting A). The calculation curves for P_x at Setting G are flat with respect to ϕ_{pq} , whereas the data suggest otherwise, as reflected by the non-zero b_x in the fits.

$${}^1\text{H}(e, e'\vec{p})$$

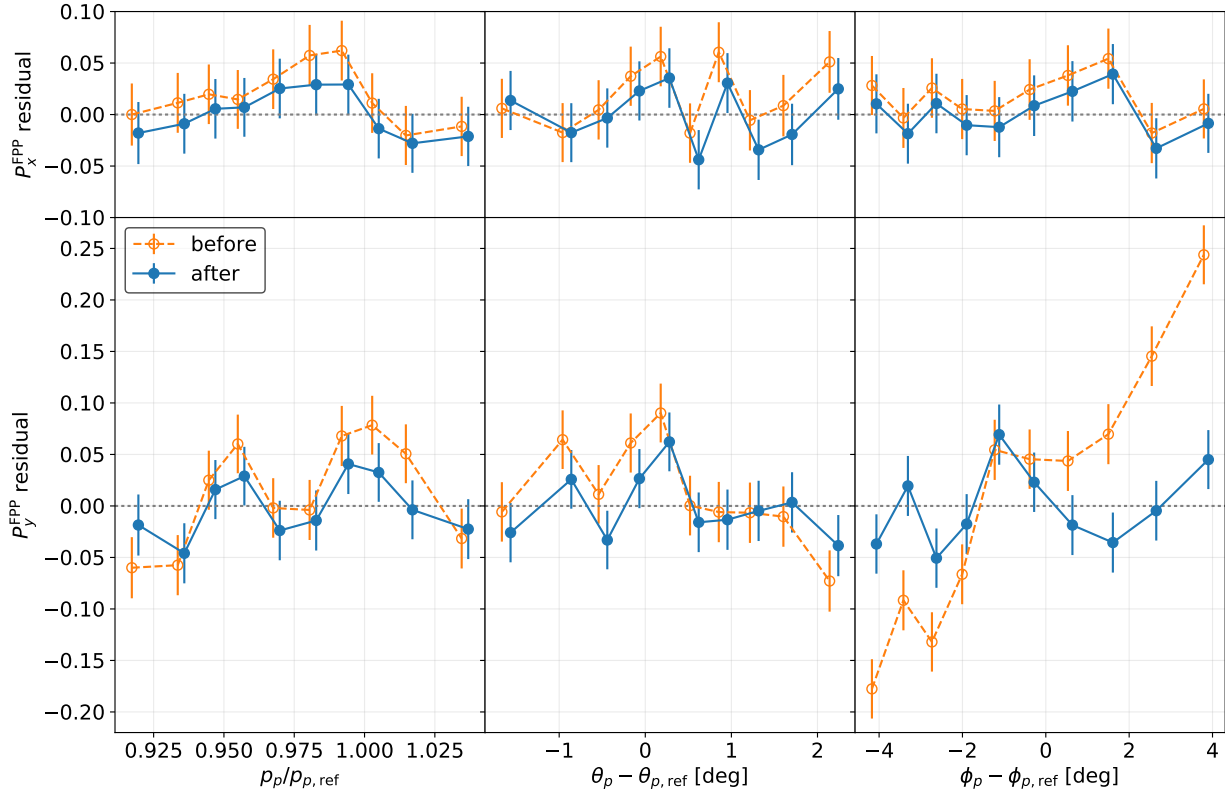


Figure S.1: The residual induced polarizations in focal-plane coordinates, P_x^{FPP} (top panels) and P_y^{FPP} (bottom panels) measured for ep scattering, without (orange, open circles, connected by a dashed line) and with (blue, filled circles, connected by a solid line) corrections for the false asymmetry. These are presented in slices of the relative momentum of the proton (left), polar angle (middle), and azimuthal angle (right)

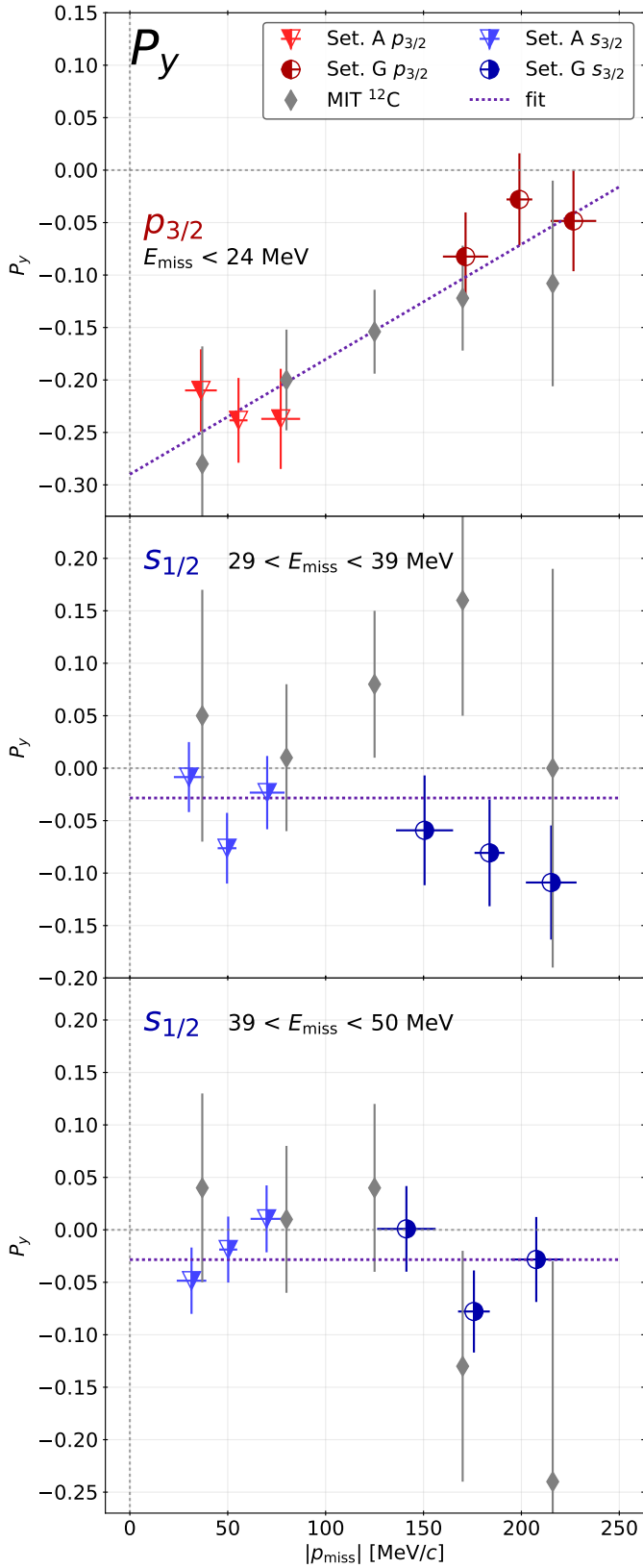
$^{12}\text{C}(e, e'\vec{p})$


Figure S.2: Comparison between the measured P_y for near-coplanar ($\phi_{pq} \approx 180^\circ$) events in this work and the MIT measurements [14]. The cut used in our data for this plot was $|\phi_{pq}| > 135^\circ$. Following [14], the events have been partitioned in slices by E_{miss} . A purple dotted line indicates a combined fit of our data with those of [14].

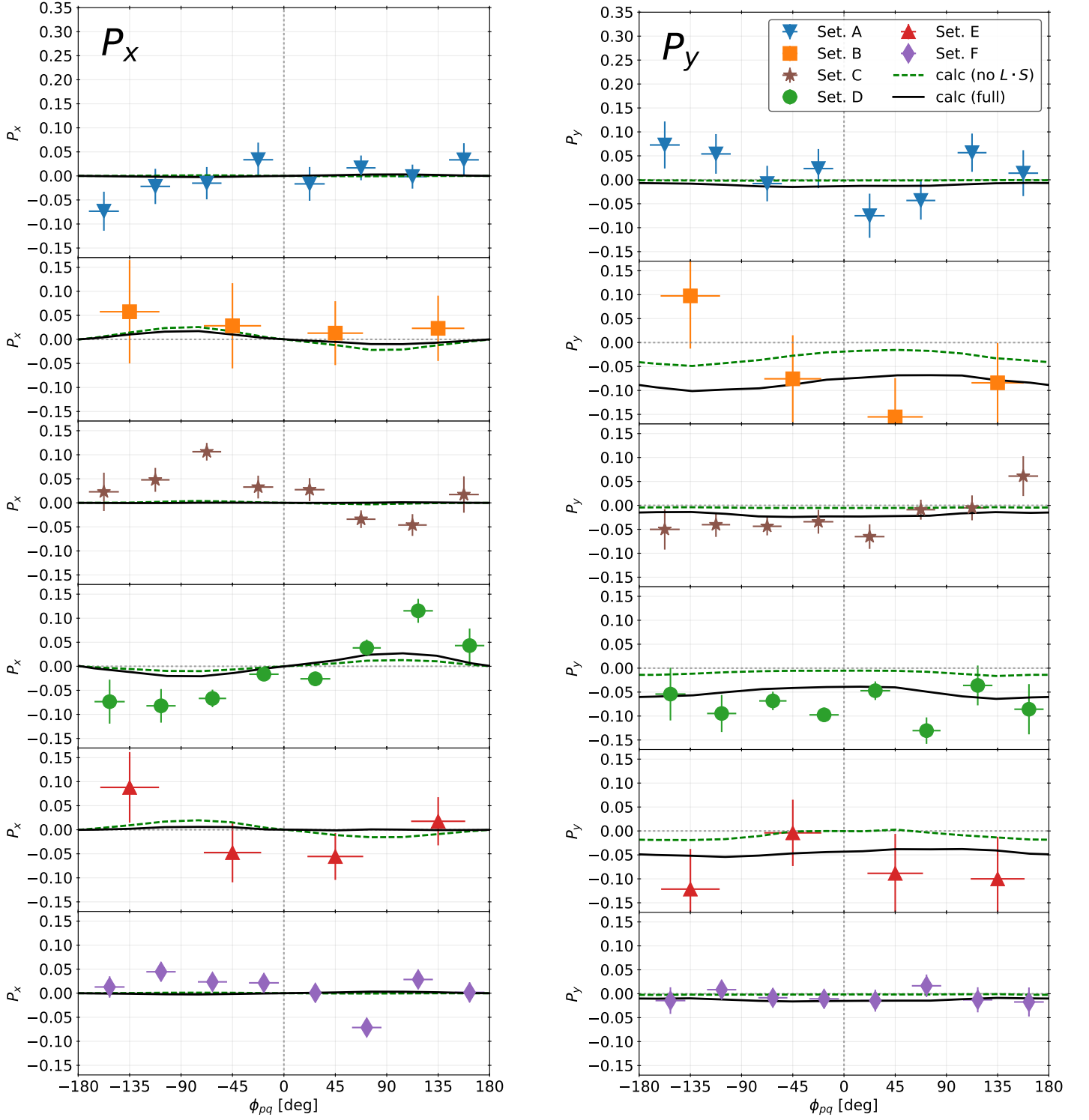
${}^2\text{H}(e, e'\vec{p})$


Figure S.3: The measured induced polarizations, P_x (left panels) and P_y (right panels) for ${}^2\text{H}$, plotted versus ϕ_{pq} . The data are shown on separate panels for each kinematic setting. The calculations with (without) the $L \cdot S$ interaction are shown as solid black (green dashed) curves.

$^{12}\text{C}(e, e'\vec{p})$

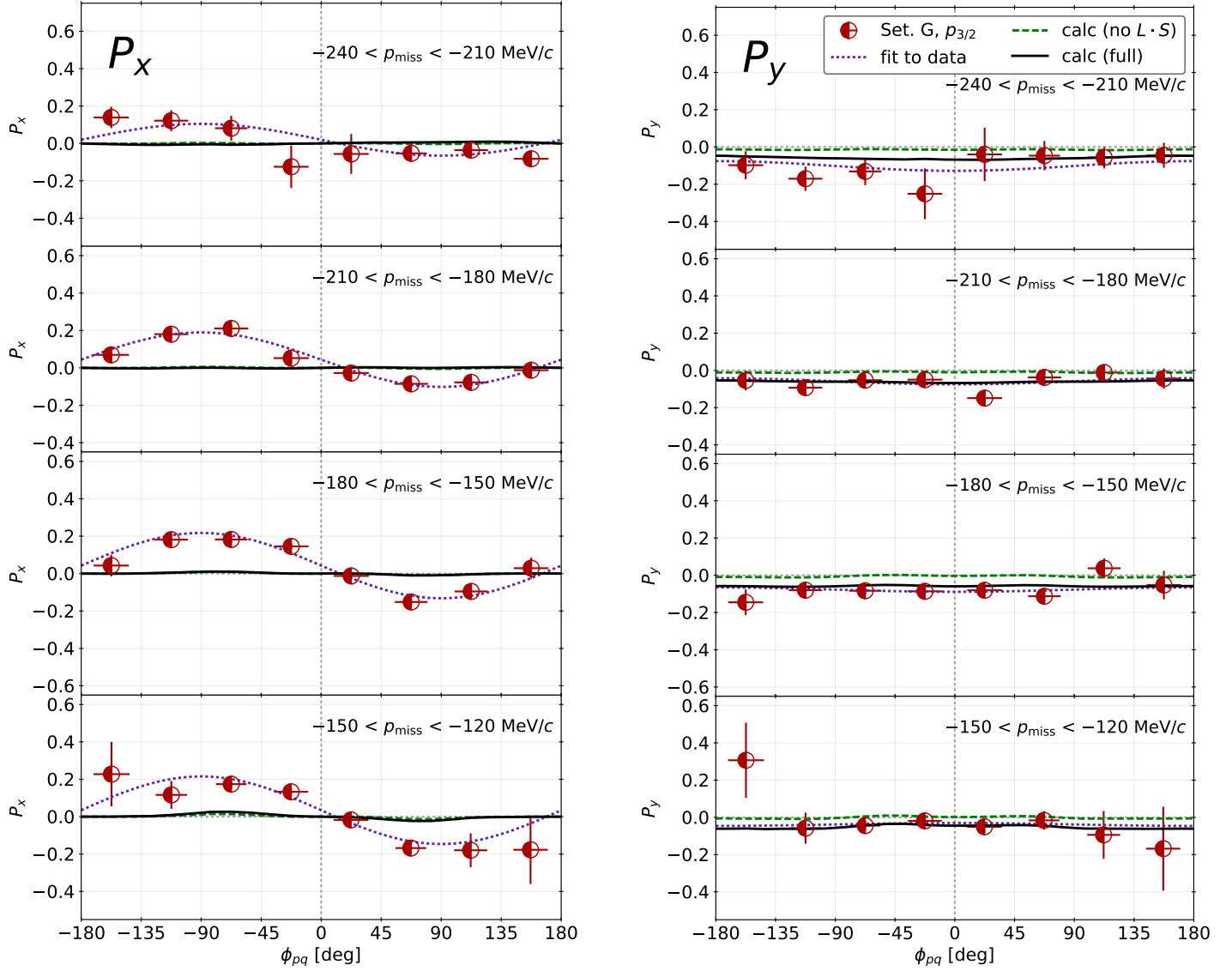


Figure S.4: P_x (left panels) and P_y (right panels) as functions of ϕ_{pq} , in several slices of p_{miss} for the p -shell knockout in ^{12}C at Setting A. The calculations with (without) the $L \cdot S$ part of the optical potential are shown as solid black (green dashed) curves. Fits of the data to $P_x = a_x + b_x \sin(\phi_{pq})$ and $P_y = a_y + b_y \cos(\phi_{pq})$ are shown for each slice (purple dotted curves).

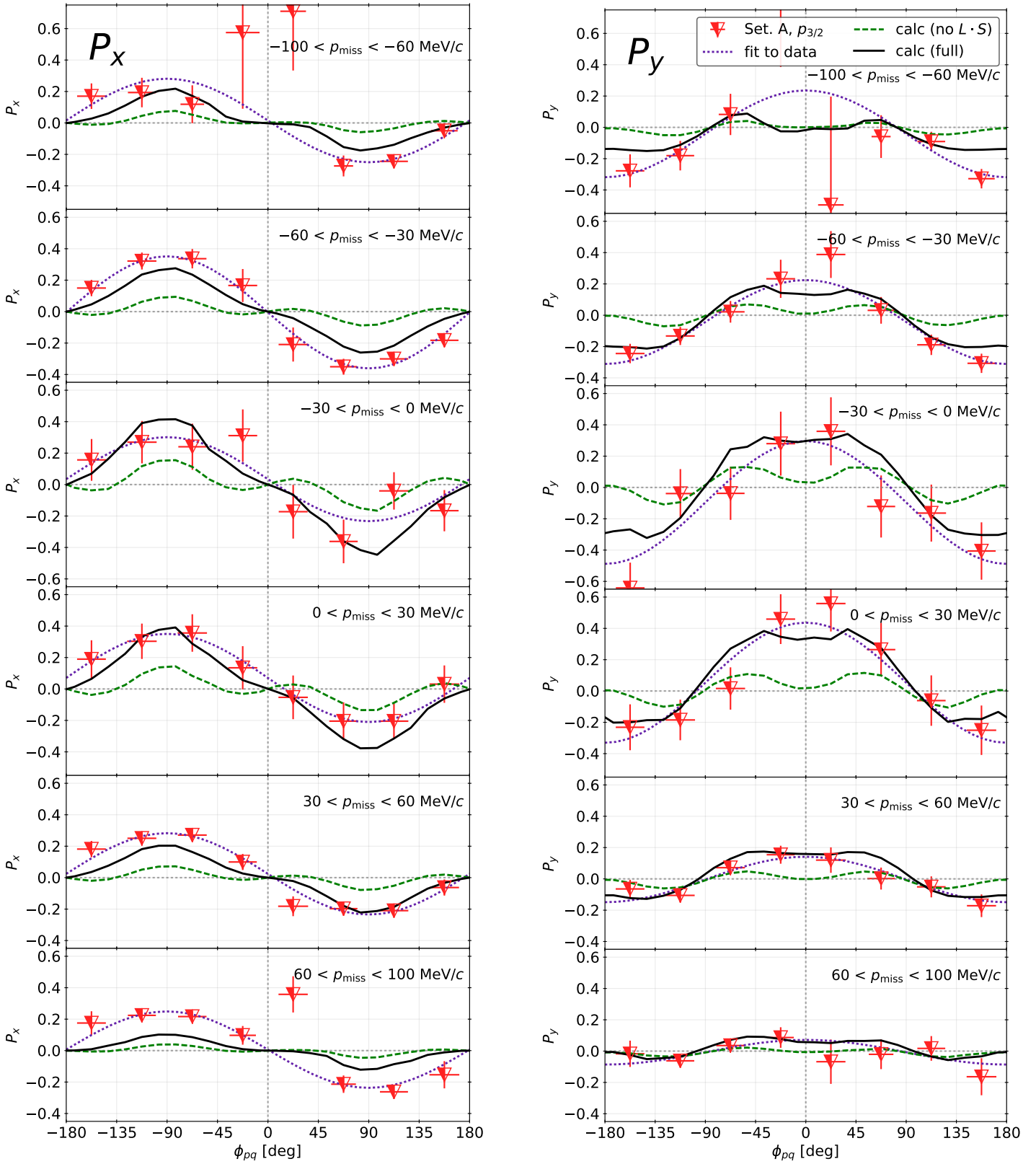
$^{12}\text{C}(e, e'\vec{p})$


Figure S.5: Same as Fig. S.4, for Setting A.

$^{12}\text{C}(e, e'\vec{p})$

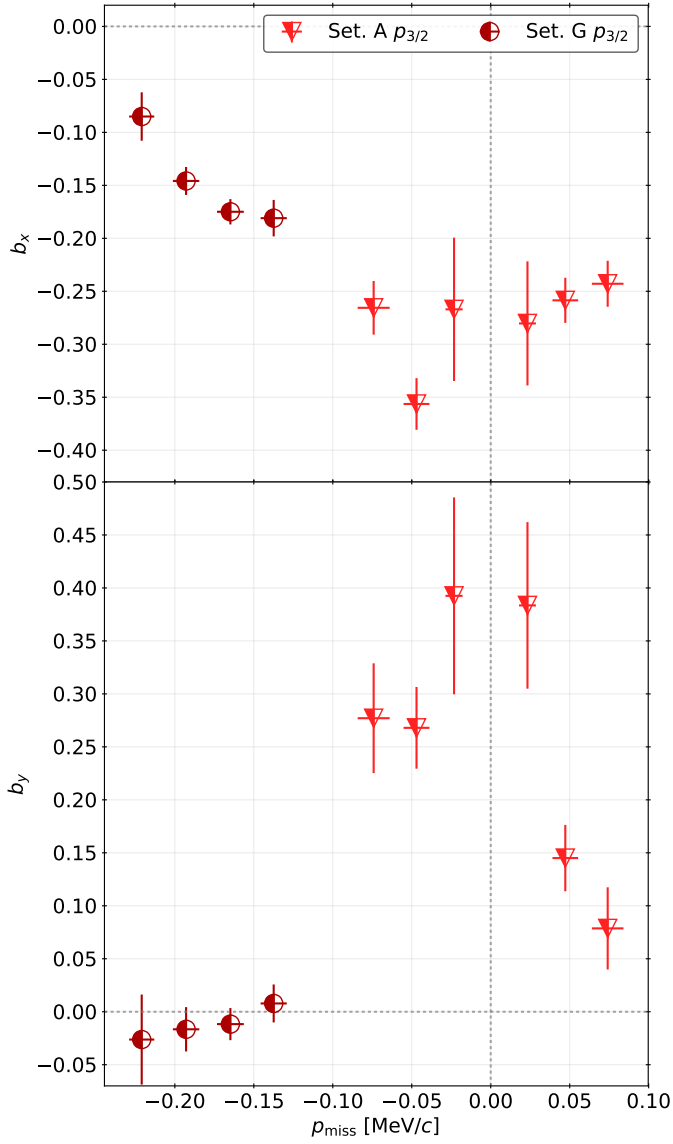


Figure S.6: The parameters b_x and b_y from the fits $P_x = a_x + b_x \sin \phi_{pq}$ and $P_y = a_y + b_y \sin \phi_{pq}$. These parameters describe the ϕ_{pq} dependence of P_x and P_y respectively.